(Received 20 January 2025, Accepted 27 February 2025, Scheduled 11 March 2025)

Wide-Band Pattern Nulling in Phased Array and Phased Array-Fed Reflector Antennas

Arun K. Bhattacharyya*

Independent Scholar, California, USA

ABSTRACT: The paper presents array-pattern synthesis for wide-band nulling at specified directions. The projection matrix method is invoked to obtain an orthogonal operator matrix (OOM). The OOM transforms a quiescent excitation vector to an optimally modified excitation vector that warrants ideal nulls at the desired directions at multiple frequencies. However, the modified excitation does not provide the optimal solution for a shaped beam, particularly near the edge-of-coverage region. We obtain an improved shaped beam solution by determining a complete set of orthonormal basis vectors that represent the column space of the OOM. Optimum amplitudes of the basis vectors yield an improved shaped beam. The method is amended for nulls in phased array-fed reflector (PAFR) antenna patterns. The method does not require the explicit determination of eigenvalues and eigenvectors, thereby enhancing the computation efficiency facilitating easy implementation in a digital processor. As a consequence, real time nulling in phased arrays and PAFRs are feasible with minimal computation burden, appealing to communication satellites.

1. INTRODUCTION

Generally, pattern nulls are created at jammer or interferer locations to improve the received signal quality. In order to accommodate the nulls in the radiation pattern, the quiescent excitation vector (weight vector) of an array is modified suitably. In a jamming scenario, the modification needs to be implemented instantaneously for an unperturbed operation, which necessitates the fast determination of updated excitation vectors. Therefore, it is of utmost importance to use a computationally efficient algorithm.

For array pattern nulling, several computational algorithms and associated adaptive array architectures are available in the open literature [1, 2]. The simplest algorithm is the Gradient Search (GS) method [3, 4], which is also known as Newton's method. Here, the problem is viewed as a "pattern synthesis" problem with peaks and nulls in the desired pattern function. Although the GS algorithm is analytically simple, it is computationally time consuming because the algorithm involves many partial derivative computations. For a large array, the computation time increases exponentially, which may not be appropriate to mitigate a real time jammer issue. In addition, the algorithm often suffers from local minima problem. A simplified version of the algorithm is employed by Kogan to obtain a deep null in a square-kilometer array [4]. The method minimizes the beam power at a single interference direction. Another approach, for wide-area nulling for pencil beams, is presented by Sayidmarie and Mohammed [5]. In this approach, the amplitudes of the edge elements are adjusted appropriately to cancel out a sidelobe peak, creating a wide-null in the sidelobe region. Due to the limited degrees of freedom, multiple nulls for multiple users may not be achievable always. In [6], Steyskal et al. presented an exhaustive review of array pattern nulling, including a generalized version of [5]. The nulls are mostly considered in the sidelobe region of the quiescent pattern and are imposed by introducing "cancellation beams". The general method is computationally efficient as the number of unknowns, which is equal to the number of cancellation beams, is small.

There is another class of algorithms that relies on the elimination of excitation vector components that lie on the null steering vector space. The simplest one is using Gram-Schmidt orthogonalization of the null steering vectors, followed by the elimination of the "orthogonalized" components from the quiescent excitation vector [7, 8]. In [7], Yuen used an auxiliary channel configuration for sidelobe cancellation adaptively. Here, the author employed a modified Gram-Schmidt orthogonalization method [9] for obtaining the complex amplitudes of the auxiliary channel. Liu et al. [8] employed a similar approach for sidelobe cancellation of a fully adaptive array. Gabriel [10] presented a spectral estimation method for low sidelobe and tracking arrays. Based on the eigenvector decomposition of covariance matrix, an adaptive algorithm nulls out the interference sources. In [11], Subbaram and Abend employed subspace separation technique for interference suppression using orthogonal projection. The method involves singular value decomposition to determine jammer subspace. In [12], Ellingson and Hampson obtained a deep null at the interference direction for radio telescope applications. The method involves the estimation of eigenvectors of the interferer-subspace followed by spatial projection for nulling. In principle, the aforementioned methods presented in [10–12] are similar, which involve explicit determination of eigenvalues and eigenvectors of the covariance matrix. The determination of eigenvalue and eigenvector of a large complex matrix may incur computational complexity, which is

* Corresponding author: Arun K. Bhattacharyya (painta9@aol.com).

not desirable in a real time jamming scenario. Iterative algorithms using successive projections are also employed for beam shaping and array nulling [13–16]. Refs. [14] and [16] deal with general principle of successive projections including its convergence properties. In [15], the method is used for achieving near field nulls, while maintaining a desired mask pattern in the coverage and near-in sidelobe regions. The imposed nulls are considered at far angular locations from the coverage region; as a result, the desired pattern shape is achieved without difficulty. In [17], genetic algorithm is employed to synthesize array pattern with nulls using element position perturbation. However, the position perturbation is not practical in a real time scenario. In [18], low sidelobe array beams are used as the basis functions for sector nulling. The method belongs to the general framework of pattern nulling discussed in [6].

Typically, horns, patches, or wideband Vivaldi elements are used as elements of an array antenna. Recently, non-conventional elements used in small arrays are proposed. In [19], an eight-element array using T-shaped patch radiator is reported for 5G applications. In [20], a high gain dielectric rod antenna excited by spoof surface plasmon polaritons based feed is proposed for extremely high frequency application.

In this paper, we employ the general framework of projection matrix method [21] for array nulling at a finite number of far field locations at multiple frequencies to cover a finite bandwidth. The method involves the determination of an orthogonal operator matrix (OOM), whose columns span the orthogonal complement of the null steering vector space. An OOM operated on a quiescent excitation vector yields a modified excitation vector. The modified excitation vector produces a pattern that warrants perfect nulls at the desired directions. The null steering vector set determines the OOM. The method does not require any eigenvector computation; hence it is computationally efficient to mitigate interferers or jammers in real time. For a pencil beam, unlike the Gram-Schmidt method, the present method does not require explicit computations of orthogonal vectors and thus, easy to implement in a digital processor. The method is extended for ideal nulls at multiple discrete frequencies, which can be used for wide-band nulling purpose. It is found that the method works perfectly for pencil beams where the maximum possible user gain is desired. However, for a shaped beam or a low sidelobe beam, the method shows a substantial deterioration of the modified pattern from the quiescent pattern. In order to improve the pattern, we determine the orthonormal basis vectors in the column space of the OOM and then obtain the optimum amplitudes for the basis vectors. We emphasize here that our proposed method produces ideal nulls, unlike the iterative approaches used in [13–16]. We suitably modify the OOM method to apply in array-fed reflector systems. Numerical examples of various pencil beams and shaped beams validate the method. We also study the effects of the imposed nulls on the array-gain.

We organize the rest of the paper as follows. In Section 2, we present the analytical foundation of the OOM method. We also include an extension of the OOM method for shaped and low sidelobe beam patterns with discrete nulls. Section 3 presents the extension of OOM method for multiple frequencies and subsequently for wide band nulling. Section 4 demonstrates the application of OOM for array-fed reflectors. Finally, in Section 5, we outline important conclusions.

2. ORTHOGONAL OPERATOR MATRIX METHOD

Consider an array antenna of N elements as schematically shown in Fig. 1. Suppose that the array elements are excited with complex amplitudes $A_1, A_2, ..., A_N$ that can be expressed by a complex vector of dimension N. For matrix manipulation purposes, the excitation vector can be treated as an $N \times 1$ column matrix denoted by $[A]$. Suppose that (x_n, y_n) is the coordinate of the nth element with respect to the coordinate system shown in Fig. 1. Then, the array factor can be expressed as

$$F = [T]\,[A] \tag{1}$$

where $[T]$ is a row matrix of order $1 \times N$, and the nth element of $[T]$ is given by

$$T_n = \exp\{jk\sin\theta(x_n\cos\phi + y_n\sin\phi)\}, \quad n = 1, 2, ..., N \tag{2}$$

In the above equation, $j = \sqrt{-1}$, $k = \frac{2\pi}{c}$; θ and ϕ are the elevation and azimuth angles of the far field radiation direction in spherical coordinate system; f is the frequency; c is the speed of light. A time dependent factor $\exp(j\omega t)$ is assumed and suppressed. Note that for a given excitation vector $[A]$, F is proportional to the far field intensity. For the exact far field intensity, one should multiply the divergence factor $\exp(-jkr)/r$, with r as the radial distance and the element pattern $ep(\theta, \phi)$ with F. However, in the present context, those two multiplicative factors are unimportant because they have no influence on the null direction.

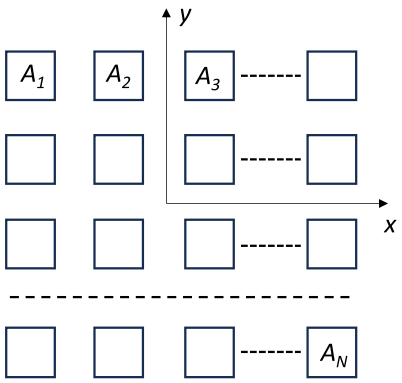

FIGURE 1. Schematic of a direct radiating array of N elements. Square-shaped elements are considered in the schematic. The quantity inside an aperture represents the excitation coefficient.

Our objective is to determine an optimum excitation vector[1] $[A]$, such that F vanishes in the desired null direction $(\theta_{\text{null}}, \phi_{\text{null}})$. We allow a small perturbation in the quiescent excitation vector to fulfill the above objective. For example, consider the quiescent excitation vector as a uniform vector (with identical elements) for a desired radiation along boresight. The uniform excitation, while ensuring maximum gain along bore-

[1] Henceforth we also use the word "vector" to represent a row or column matrix.

sight, does not guarantee a null along $(\theta_{\text{null}}, \phi_{\text{null}})$ direction. Hence, the excitation vector needs to be modified for creating a null along $(\theta_{\text{null}}, \phi_{\text{null}})$, with a minimum reduction in gain along boresight.

For generality, we assume multiple null directions. In that situation, (1) should be generalized as

$$[F] = [T]\,[A] \tag{3}$$

Here, $[F]$ should be a column matrix (a vector) of order $K \times 1$, where K is the number of null directions. Accordingly, $[T]$ should now be a matrix of order $K \times N$, and the elements of $[T]$ should be given by

$$T_{in} = \exp\{jk \sin\theta_i (x_n \cos\phi_i + y_n \sin\phi_i)\}, \tag{4}$$

with $i = 1, 2, ..., K$ and $n = 1, 2, ..., N$. In (4), (θ_i, ϕ_i) is the ith null direction.

It is important to note that for perfect nulls, $[F]$ should be a null vector. This implies that every row vector of the $[T]$ matrix should be orthogonal to the row vector $[A]^H$, where the superscript "H" denotes Hermitian operator (transpose operator after complex conjugation of the elements). We introduce the "Hermitian operator" because in the complex domain the inner product of two vectors $\vec{P}$ and $\vec{Q}$ is defined as $\vec{P} \cdot \vec{Q} = \sum p_i q_i^*$, whereas, in the conventional matrix multiplication, the complex conjugation $(*)$ is not used. Here, p_i and q_i represent the ith components of the vectors $\vec{P}$ and $\vec{Q}$, respectively.

Now consider a row vector $[V]$. The projection vector of $[V]$ that lies on the row space of $[T]$, denoted as $[V_T]$, can be represented by a linear combination of the row vectors of $[T]$. Mathematically,

$$[V_T] = p_1\,[T_1] + p_2\,[T_2] + p_3\,[T_3] + \cdots + p_K\,[T_K] \tag{5}$$

In the above, p_i is a complex number, and $[T_i]$ is the ith row of $[T]$, where i assumes values from 1 to K. In matrix format, (5) can be expressed as

$$[V_T] = [P]\,[T] \tag{6}$$

Here, $[P]$ represents a row matrix with elements as $p_1, p_2, ..., p_K$. The component of $[V]$, which is orthogonal to the row space of $[T]$, can be expressed as

$$[V_O] = [V] - [V_T] = [V] - [P]\,[T] \tag{7}$$

Since $[V_O]$ is orthogonal to the row space of $[T]$, we must have

$$[V_O]\,[T]^H = [0] \tag{8}$$

The righthand side of (8) represents a null vector. Combining (7) and (8), we obtain

$$[V]\,[T]^H - [P]\,[T][T]^H = [0] \tag{9}$$

Now, $[P]$ can be determined from (9), which is given by

$$[P] = [V]\,[T]^H[[T][T]^H]^{-1} \tag{10}$$

Substituting the above expression for $[P]$ in (7), the orthogonal vector $[V_O]$ is obtained as

$$[V_O] = [V]\,[[I] - [T]^H[[T][T]^H]^{-1}\,[T]] \tag{11}$$

Here, the term $[I]$ represents a unit matrix of order $N \times N$. The matrix $[I] - [T]^H[[T][T]^H]^{-1}[T]$ is the "orthogonal operator matrix (OOM)" associated with the orthogonal complement of the row-space of $[T]$. The quantity $[T]^H[[T][T]^H]^{-1}[T]$ is the "projection operator matrix" [21].

The problem at hand is to determine the excitation vector $[A]$ such that the left-hand side of (3) becomes a null vector. Toward that end, we set $[V]$ as the Hermitian transpose of the quiescent excitation vector. Then, the desired excitation vector, which is the perturbed version of the quiescent excitation vector, should be given by

$$[A] = [V_O]^H = [[I] - [T]^H[[T][T]^H]^{-1}\,[T]]^H\,[V]^H \tag{12}$$

The right-hand side term can be simplified, yielding

$$[A] = [[I] - [T]^H[[T][T]^H]^{-1}\,[T]]\,[V]^H \tag{13}$$

It can be verified from (13) that $[T][A] = [0]$. It should be mentioned here that the angular deviation of the modified excitation vector $[A]$ from the quiescent excitation vector $[V]^H$ is minimum (see the Appendix for a proof). This leads to an interesting conclusion in regard to a *quiescent excitation with uniform taper and linear phase*. The "modified excitation vector" will exhibit the highest possible user gain with discrete nulls because the steering vector along the user direction is the same as the complex conjugate of quiescent excitation vector within a constant multiplier.

It is worth noting here that the right-hand side of (13) involves simple matrix multiplications. Consequently, the computational burden for obtaining the OOM (hence, determination of the modified excitation) is minimal. Unlike in [10], there is no need for eigenvalue/eigenvector analysis. Although there is a matrix inversion involved in the present formulation, the matrix is of very low order ($K \times K$ for K nulls), regardless of the array size N, and the matrix is generally very well conditioned.

To demonstrate, (13) is employed to create a null in the patterns of a linear array of 10 elements. The element size is $1.5\lambda \times 1.5\lambda$, where λ denotes the wavelength. We consider the radiating elements as uniform current sources with 100% aperture efficiency. The desired radiation is along the boresight (user location). In order to maximize user gain, we consider a uniform taper for the quiescent excitation; hence $[V]$ is a 1×10 matrix with identical elements. We employ Equation (4) to construct the $[T]$ matrix. Fig. 2 shows the quiescent pattern and the two modified patterns with desired discrete nulls at (2°, 0) and (5.6°, 0), respectively. The null at (2°, 0) is located at the main lobe of the quiescent beam. Note that to create the null, the beam-peak shifts to the left. As a result, the gain at boresight decreases by about 2 dB for this case. Fig. 3 shows the ampli-

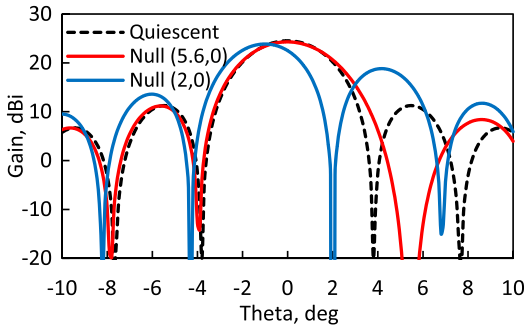

FIGURE 2. Quiescent and modified patterns with one null each.

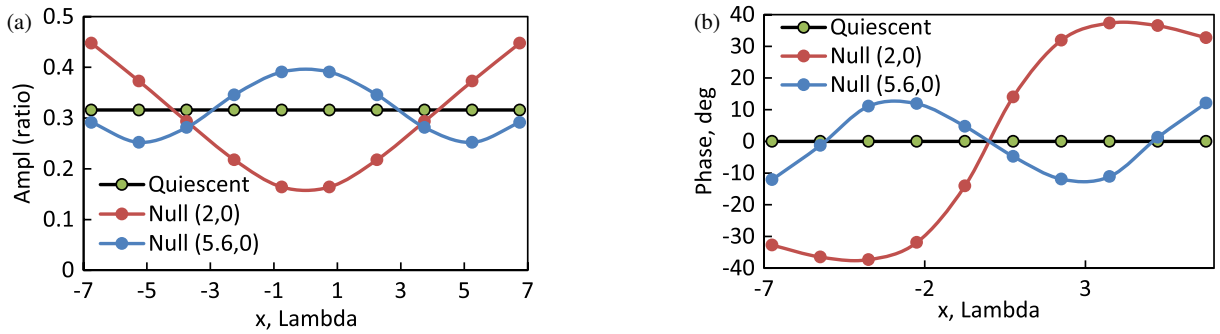

FIGURE 3. Amplitude and phase distributions of 10-element linear array. (a) Amplitude, (b) phase.

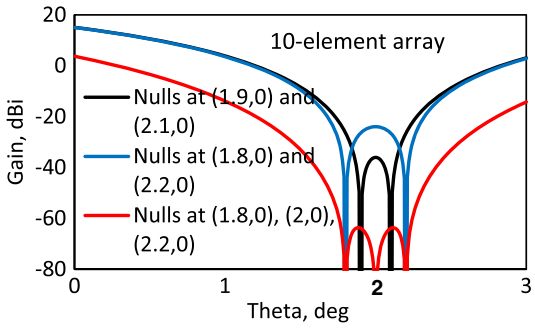

FIGURE 4. Sector nulling with two and 3 discrete nulls.

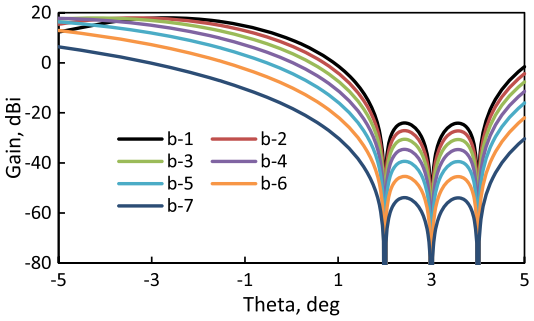

FIGURE 5. Seven orthogonal beams of a linear array of 10 elements. Each beam has nulls at three fixed discrete points.

tude and phase distributions of the modified excitation. It has 9 dB amplitude taper with almost a linear phase progression. In fact, the modified pattern is the superposition of the quiescent pattern and a scanned-beam pattern along $(2^\circ, 0)$ scan direction, which conceptually concurs with the results presented in [6]. The amplitude vector associated with the "scanned" beam pattern is the projected vector onto the null steering vector. The superposition of two such amplitude vectors results in amplitude and phase taper. In the second example, the desired null is located at the first sidelobe adjacent to the main beam. In this case, the beam peak does not shift, but the main lobe is broadened to the right-hand side. Here, the gain reduction at boresight is only about 0.2 dB. The amplitude taper is about 4 dB, and the phase pattern is not monotonic.

2.1. Sector Nulling

The algorithm can be employed to produce a beam with very low gain (specified as null-depth) inside a region of interest (sector nulling). In that situation, multiple closely spaced discrete nulls should be considered inside the region, and then an optimum excitation vector can be determined. The gain between the discrete null points does not vanish; however, it should be sufficiently low for all practical purposes. The allowable "null-depth" inside the region determines the interval between the discrete null points. For a large null-depth requirement, the interval between two successive discrete nulls should be narrow, as the peak "sidelobe" gain between the discrete nulls is almost proportional to the interval-length in $\sin\theta$ domain [13, p. 28]. Accordingly, the number of discrete nulls inside the sector should be increased for achieving a larger null-depth.

Another important point should also be considered in deciding the number of discrete nulls, particularly in the main lobe region. Although the null-depth improves with the number of discrete nulls, the user gain deteriorates as the number of zeros in the "array factor" increases. The slope of the gain curve in the vicinity of the nulls decreases with the number of zeros; hence the gain at the user location does not recover to the quiescent value, which is demonstrated in Fig. 4. Here, the array patterns with 2 and 3 nulls inside a sector are shown. For the 2-null cases, the results indicate that the "sidelobe" gain between the discrete nulls increases by about 12 dB when the null-interval doubles. The user gain at (0, 0) slightly changes. For the 3-null case, the sidelobe gain decreases significantly, but the user gain deteriorates as the gain slope decreases substantially. It should be mentioned here that although multiple discrete nulls with low spacing improve the null depth inside the sector, the expected value of the null depth, considering amplitude and phase tolerances, may not improve as much.

2.2. Shaped and Low Sidelobe Beams with Nulls

The methodology can be extended with an additional step to construct multiple user beams or shaped user beam while maintaining discrete nulls at the specified points. Toward that end, a set of orthogonal amplitude vectors, each of which produces perfect nulls at the specified points, needs to be determined first. A linear combination of the orthogonal vectors with optimum weights yields the desired gains at the user locations or a shaped

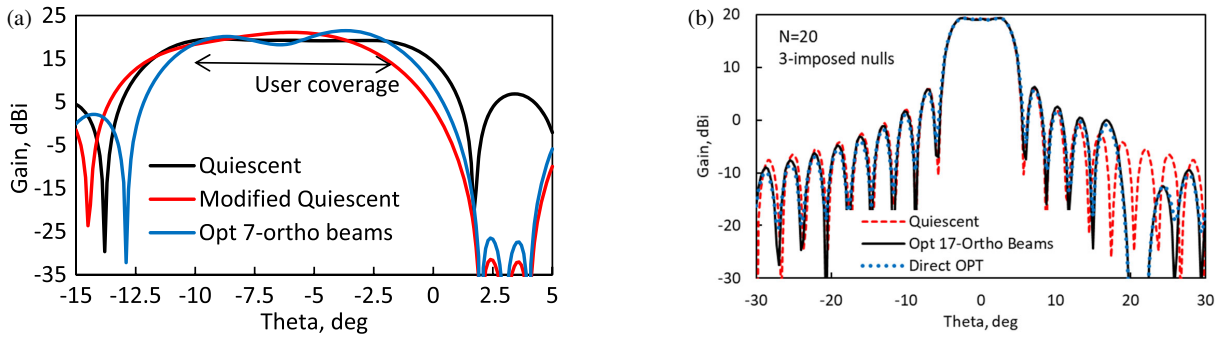

FIGURE 6. Shaped beams with nulls at fixed discrete points. (a) 10-element linear array, element size $= 1.5\lambda_0 \times 1.5\lambda_0$, (b) 20-element linear array, element size $= \lambda_0 \times \lambda_0$.

beam while maintaining perfect nulls at the specified points. In order to determine the set of the orthogonal amplitude vectors, two methods can be employed. The simplest one is directly using the OOM in (11). Note that each column vector of the OOM, $[I] - [T]^H[[T][T]^H]^{-1}[T]$, represents an excitation vector that yields perfect nulls at the specified points. The Gram-Schmidt orthogonalization of the column vectors [21] yields the complete set of orthonormal (with unit norm) basis vectors. It should be mentioned here that the number of basis vectors should be equal to $(N - K)$, which is equal to the rank of the OOM.

To demonstrate the above method, we first determine the orthonormal set of excitation vectors for a 10-element linear array with 3 discrete nulls located at (2°, 0), (3°, 0), and (4°, 0), respectively. The element size is $1.5\lambda \times 1.5\lambda$. The number of orthogonal excitations should be equal to 7 for this case. The orthogonal beams, associated with orthogonal excitations, are computed. Fig. 5 shows 7 orthogonal beams[2]. Note that the 7 beams in this case span the entire far field space with 3 fixed nulls. Hence, an arbitrary beam constructed with a linear combination of the orthogonal beams will preserve the null locations. In order to optimize the flat-top shaped beam, we need to determine appropriate weights of the orthogonal beams. For only one user location, the weights are simply the complex conjugates of the complex far field intensity. For multiple user locations or for a shaped beam, the beam-weights can be determined using a gradient search or conjugate field matching algorithms [13]. From the beam-weights, one can easily determine the element-weights in a straightforward manner.

Figure 6(a) shows the quiescent shaped beam (flat-top beam) covering (−10°, 0) to (−2°, 0) and the modified beams with deep nulls at (2°, 0), (3°, 0), and (4°, 0), respectively. We obtain the quiescent excitation by employing a conjugate field matching optimizer [13] and achieve a minimum gain of 19.06 dBi inside the "flat-top" region. Then using (13), the quiescent excitation is modified to create nulls at the desired locations, and the pattern is computed with the modified excitation. Noticeably, the "modified quiescent" pattern moves to the left (away from the nulls), which results in a 4.1 dB lower gain near (−2°, 0) coverage-edge. The worst-case isolation between the user coverage region and null region (between (2°, 0) and (4°, 0)) is about 46.3 dB. Next, we employ the set of 7 orthogonal excitation functions to reshape the flat-top pattern. The pattern shows a significant improvement in regard to the edge-of-coverage gain. The worst-case gain inside the coverage region is only about 0.8 dB lower than that of the quiescent beam, which corresponds to a 3.3 dB improvement from the "modified quiescent" beam. The worst-case isolation for this case is 44.7 dB, which is about 1.6 dB lower. The somewhat lower gain performance is due to the reduced degree of freedom by the number of nulls.

In Fig. 6(a), although we improve the coverage gain significantly, the reshaped beam is somewhat different from the quiescent beam. This is due to the insufficient degree of freedom for optimization and the proximity of the imposed null from the coverage region. If, however, the imposed null locations are far from the coverage region, and/or the number of orthogonal beams increases (which is equal to the number of elements minus the number of imposed nulls), then the reshaped beam should have less deviation from the quiescent beam. This is demonstrated in Fig. 6(b). Here, we consider a 20-element linear array with element size $\lambda \times \lambda$, and the imposed null locations are set at 20°, 21°, and 22°, respectively. The coverage region extends from −3° to 3°. Evidently, the optimized pattern shape closely follows the quiescent beam, while creating deep nulls at the desired angles.

To validate the method, we compare the computed pattern with that obtained using the conjugate field matching algorithm (CFM) [13] for the 20-element array. The CFM algorithm directly optimizes the shape of the beam iteratively. We consider 12 far-field sample points in the coverage region and 3 far-field samples points at the null locations with assigned null-gain of −60 dBi. In Fig. 6(b), we include the results of the optimized pattern. The gain difference in the coverage region lies within ±0.06 dB. Between the null locations, the difference is about ±2.0 dB at −40 dBi level. Exactly at the null locations, the optimizer yields −58 dBi gain, which is very close to the desired value. The good match between the patterns confirms the accuracy of the present method.

It should be mentioned here that generally the modified excitation using (13) does not maintain the low sidelobe levels of the quiescent beam, as indicated in Fig. 2. For maintaining

[2] Orthogonality is not apparent from the plot because only a small portion of the patterns are shown.

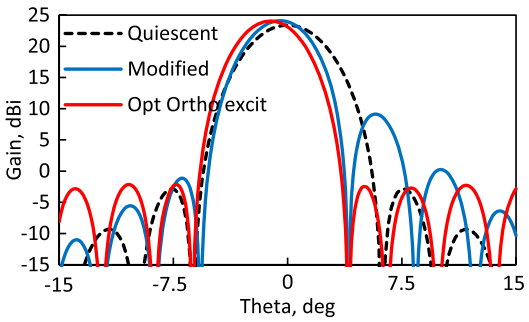

FIGURE 7. Sidelobe optimization using orthogonal excitations.

low sidelobe levels (in addition to the nulls in the specified locations), amplitudes of the orthogonal excitation vectors need to be optimized. The optimization is performed for a quiescent pencil beam, and the results are depicted in Fig. 7. Here, in addition to the quiescent beam pattern, we plot two beam patterns, each of which has a discrete null at (4°, 0). The quiescent beam corresponds to a cosine excitation on a pedestal, yielding about 26 dB side lobe level with a peak gain of 23.4 dBi. When the quiescent excitation is modified using (13) for imposing a discrete null at (4°, 0), the gain increases to 23.9 dBi, but the sidelobe deteriorates to about 15 dB level. As mentioned, we then optimize the amplitudes of the orthogonal excitation vector to obtain low sidelobe levels within $\pm 15°$ visible range. The optimized beam shows 23.1 dBi user gain, with a sidelobe level about 25.5 dB. Although the user gain is reduced by 0.8 dB, the sidelobe level is improved by 10.5 dB, which is very substantial from the application point of view.

Another method, using the eigenvectors of the OOM, can also be employed for reshaping the beam. Because the OOM is Hermitian, the eigenvectors are orthogonal, which represent the desired set of orthogonal vectors. Here also the number of nonvanishing eigenvectors should be equal to $(N - K)$ as K eigenvalues vanish identically due to lower rank of the matrix. In principle, the final result should be identical as the eigenvectors represent only an "alternate set of orthogonal basis vectors". Moreover, the determination of eigenvectors is computationally expensive, particularly for a large array and may not be preferable for some applications.

To examine the computational efficiency, we compare the computation time of the present method with two prevalent array-optimization methods, viz. gradient search and conjugate field matching methods. The computer has Intel (R) processor with 32 GB RAM. We consider a pencil beam of desired peak gain at the boresight. Two null locations are considered; one at the sidelobe region and the other at the main lobe region.

TABLE 1. Computation times for generating a null by an array of 12×12 elements. Element size $= 2\lambda_0 \times 2\lambda_0$. User location is at (0, 0).

Null location (θ_{null}, ϕ_{null})	Gradient Search	Conjugate Field Match	Present Method
(2°, 45°)	21.49 sec	2.06 sec	2.08 sec
(1.5°, 0°)	21.96 sec	16.17 sec	2.14 sec

Table 1 shows the numerical results. For the imposed null location at (2°, 45°), the present method is 10 times faster than the gradient search method, while it is of the same order of the conjugate field matching method. However, for the imposed null in the main beam region, the present method is faster than other two methods. Furthermore, the present method shows ideal null (lower than -250 dBi) at the desired location, whereas the gradient search and conjugate match algorithms show -33 dBi and -85 dBi nulls, respectively. Also, the gradient search algorithm shows about 2 dB lower gain at the user location.

3. OPTIMIZATION FOR MULTIPLE FREQUENCIES

The OOM method described above is extended for multiple discrete frequencies. For this case, the $[T]$ matrix in (3) should have additional number of rows. The elements of the $[T]$ matrix should be given by

$$T_{pn} = \exp\{jk_m \sin\theta_i (x_n \cos\phi_i + y_n \sin\phi_i)\} \tag{14}$$

with $i = 1, 2, ..., K$, $m = 1, 2, ..., M$, and $n = 1, 2, ..., N$. Here, $k_m = \frac{2\pi f_m}{c}$; f_m is the mth frequency; M is the total number of discrete frequencies; and the consolidated index p is given by $p = i \times m$. Note that the order of the $[T]$ matrix is now increased to $KM \times N$, where K is the number of nulls, and N is the number of elements. The optimum excitation can be computed using (13). It should be mentioned here that in order to invert the $[T][T]^H$ matrix, the number of rows of $[T]$ should not exceed the number of columns, i.e., KM should not exceed N. If this constraint is violated, then the product matrix becomes singular, and inversion is not possible to obtain. For this case, the number of unknowns $(= N)$ exceeds the number of equations $(= KM)$; hence, the solution does not exist.

We employ the method for creating a null near a sidelobe peak of the quiescent beam for the array of 10 elements considered in Fig. 2. We consider three discrete frequencies for optimization viz. $f = 11.602$, 11.802, and 12.002 GHz, respectively, with a null at (5.6°, 0). Fig. 8 shows the radiation patterns. Ideal discrete nulls are achieved for all three frequencies. We also compare the results with single frequency optimization, optimized at 11.802 GHz. In this case, a perfect null at 11.802 GHz is achieved; however, the null depths at the other two frequencies are reduced to 35 dB and 30 dB, respectively (not shown). Furthermore, with 3-frequency optimization, the "null-width" becomes wider than the single frequency opti-

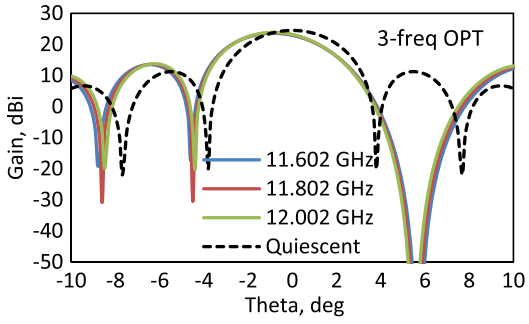

FIGURE 8. Multi-frequency optimized patterns. Null is in the sidelobe region of the quiescent beam at (5.6°, 0).

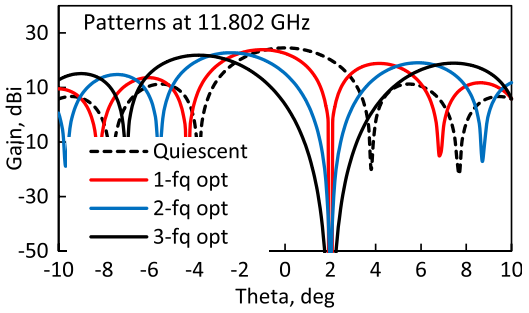

FIGURE 9. Multi-frequency optimized patterns. Null is in the main lobe of the quiescent beam at (2°, 0).

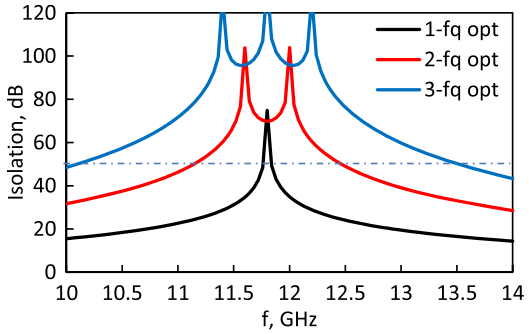

FIGURE 10. Frequency versus isolation for one, two and three frequency optimizations.

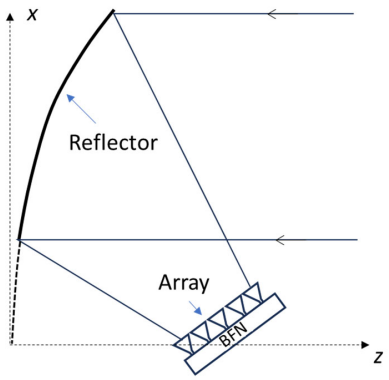

FIGURE 11. Schematic of an array-fed offset reflector (BFN stands for Beam Forming Network).

mization. The result indicates that the single frequency optimization is more susceptible to amplitude and phase tolerances than multiple frequency optimization.

To probe further, we consider a null in the main lobe of the quiescent pattern of the 10-element array. Then, we use two and three frequency optimizations and compare the results in Fig. 9. The null location is at (2°, 0). Note that as the number of "null frequency points" increases, the pattern curve becomes wider (lower slope) near the null region. In other words, a multi-frequency optimized pattern exhibits wider area-coverage than that of a single frequency optimized pattern. This is because with the array factor being a function of $k \sin\theta$, a wide-band null for a given value of $\sin\theta$ is equivalent to a wide-angle null for a given value of k (hence frequency). The reason for the "low slope" in the multi-frequency optimized pattern is due to the existence of multiple zeros in the array factor that are in close proximity, which results in lower slope near the null location.

In Fig. 9, it is important to note that the array gain at the boresight decreases with the number of optimized frequencies, when the null is considered in the main lobe of the quiescent beam. For the array under consideration, the gains at boresight are 22.5 dB, 15.1 dB, and 3.8 dB, respectively associated with 1, 2, and 3 frequency optimizations. However, the isolation (difference between boresight gain and gain near (2°, 0) for this case) improves considerably with multi-frequency optimization. Fig. 10 shows isolation versus frequency plot. A multi-frequency optimization improves not only the bandwidth but also the isolation value. For instance, 50 dB isolation bandwidths respectively are 0.7%, 11.2%, and 28.8% for 1, 2, and 3 frequency optimizations. In this context, it is worth mentioning here that the gain at the boresight location does not change considerably with the number of optimized frequencies if the desired null location is outside the main lobe of the quiescent pattern (see Fig. 8).

4. ARRAY-FED REFLECTORS

The OOM method can be employed for optimizing null beams in an array fed reflector (AFR) system shown schematically in Fig. 11. In this case, the $[T]$ matrix in (3) needs to be modified. Unlike a direct radiating array, an AFR can be viewed as an "array of dissimilar elements", because the "element pattern" (defined as the radiation pattern of the "reflector system" when only one element of the feed-array is excited while the other elements are match-terminated) varies from element to element. The composite radiation pattern of the AFR is the weighted sum of the element patterns, with the input excitation voltages as the weights. Therefore, the element T_{in} in (4) should be replaced by the complex element field in the desired null direction. Mathematically,

$$T_{in} = E_n(k, \theta_i, \phi_i), \quad i = 1, 2, ..., K \text{ and } n = 1, 2, ..., N \tag{15}$$

where $E_n(k, \theta_i, \phi_i)$ represents the complex electric field of the nth excited element along the ith null direction. The electric field is computed using the *physical optics* method. Note that, unlike in (4), here T_{in} has magnitude different from unity, and it varies with the feed-element's location. To incorporate the mutual coupling effects, the field should be normalized with respect to the incident power (assuming transmitting mode). It is worth mentioning here that for a direct radiating array mutual coupling can be incorporated using the same strategy. For multiple frequency optimization, the modification is straightforward as discussed in Section 3.

We employ the method to produce a null on the radiation pattern of an AFR. We use the following parameters for the AFR structure: Reflector's projected (projected on the z-plane) diameter $D = 50\lambda$, focal length $F = 50\lambda$, Reflector's center offset $= 30\lambda$, feed array location $= 3\lambda$ from the focus toward reflector's center, array element size $= 0.6\lambda \times 0.6\lambda$, and the number of array-elements $N = 37$. The elements are arranged

in a "stepped-circular" configuration. We first optimize the array excitation (quiescent excitation) to produce a pencil beam at the boresight of the reflector using conjugate field matching method. Essentially, the complex conjugates of the "element pattern fields" of the AFR constitute the quiescent excitation vector. Then, we employ (13) to modify the excitation vector that yields a null at (2°, 0). Fig. 12 shows the quiescent pattern and the pattern with a sharp null at (2°, 0). In order to produce a wider null, we select 3 discrete null locations, viz. at (2°, 0), (2.3°, 0), and (2.6°, 0), respectively. Fig. 12 also shows the optimized pattern. The increased null-width using multiple discrete nulls has an impact on the boresight gain. In this particular example, the boresight gain is reduced by about 0.1 dB and 1.0 dB for one and three discrete nulls, respectively. This result is very similar to that of a direct radiating array.

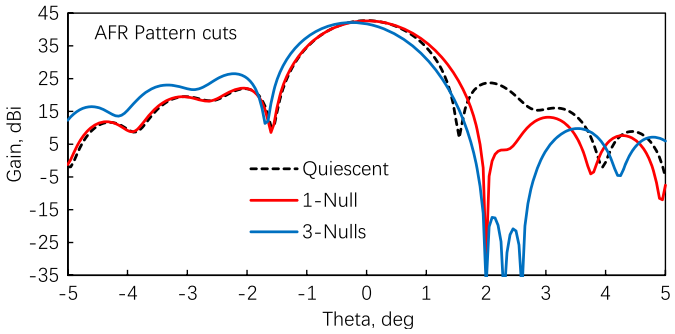

FIGURE 12. Array-fed reflector patterns for one and three nulls. The reflector diameter $D = 50\lambda$, $F/D = 1$, number of array feeds $= 37$, feed size $= 0.6\lambda \times 0.6\lambda$.

Figure 13 shows the isolation versus frequency for 1- and 3-null optimizations. The isolation data is computed at the midpoints of the null-widths. Note that the isolation bandwidth is significantly wider for 3-null optimization than 1-null optimization. For this example, the 50 dB isolation bandwidths are 4.2% and 10.2%, respectively. This behavior is very similar to that of a direct radiating array (DRA). However, unlike a DRA, only 2 spikes are observed for the 3-null case. This is primarily because unlike the array factor of a DRA, the k and $\sin\theta$ terms do not have the same footing in the resultant DRA pattern. In other words, unlike (4), the expression of T_{in} in (15) is not an explicit function of $k\sin\theta$. Consequently, for an AFR, an ideal null in $\sin\theta$ domain does not guarantee an ideal null in the k domain.

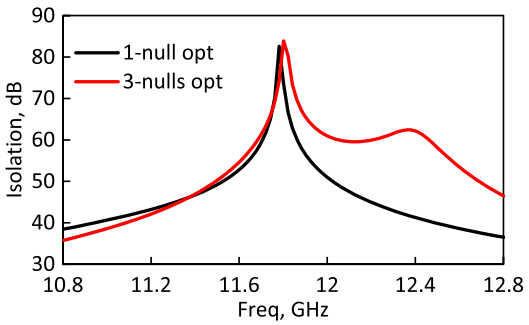

FIGURE 13. Frequency versus isolation of the array-fed reflector in Fig. 12.

5. CONCLUDING REMARKS

We obtain a matrix operator that directly transforms the quiescent excitation vector of an array pattern to a modified excitation vector, which guarantees multiple discrete nulls at the desired directions. The method is extended for multiple frequencies that allows obtaining wideband discrete nulls. It is found that a direct application of the matrix operator, operating on a quiescent excitation of uniform taper, yields the best possible user gain for a pencil beam. However, for a shaped beam the direct method shows significantly lower edge of coverage gain. In addition, the direct method deteriorates the sidelobe levels from that of the quiescent beam. In order to improve the shaped beam pattern and/or low sidelobe beam pattern, we determine the orthogonal basis vectors of the matrix operator and obtain the optimum amplitudes of the basis vectors to reshape the beam. This significantly improves the edge of the coverage gain and sidelobe levels. The method is extended for creating nulls in array-fed reflector patterns. The methodology presented here is very straightforward and easy to implement in a digital processor, which is beneficial to mitigate jamming issues in a real time situation.

APPENDIX A. PROOF OF MINIMUM DEVIATION OF THE MODIFIED EXCITATION

We consider one dimensional row space of the $[T]$ matrix in (3) to illustrate the "orthogonal space" concept by a schematic. In Fig. A1, suppose that the vector $\overrightarrow{OP}$ represents the quiescent excitation vector $[V]^H$ and that $\overrightarrow{ON}$ represents the space spanning the row space of $[T]$. The parallelogram represents the space orthogonal to the row space of $[T]$. The projection of $\overrightarrow{OP}$ onto the parallelogram is $\overrightarrow{NP}$. The vector $\overrightarrow{NP}$ essentially represents the modified excitation vector $[V_0]^H$. Now, any excitation vector that lies on the plane of the parallelogram produces nulls at the desired directions. Here, we will prove that among all possible excitations, the $\overrightarrow{NP}$ vector yields the lowest angular deviation from $[V]^H$. Toward that end, we consider an arbitrary excitation vector $\overrightarrow{RP}$ that lies on the plane of the

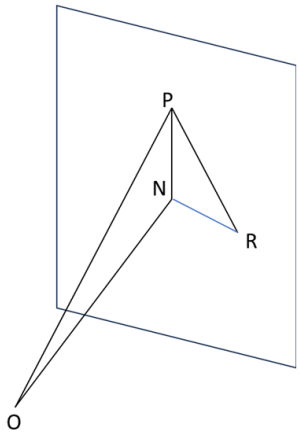

FIGURE A1. Schematic of vector space. The vector $\overrightarrow{OP}$ represents the quiescent excitation, and the parallelogram represents the space orthogonal to the row space of $[T]$ matrix.

parallelogram. The inner product of the unit vectors essentially measures the deviation in regard to the array gain. Thus, the deviation D between the quiescent excitation and the excitation that corresponds to $\overrightarrow{RP}$ should be (note, in the following equations, only the magnitudes of the complex scalar products are equated)

$$D = \frac{\overrightarrow{OP}\cdot\overrightarrow{RP}}{\left|\overrightarrow{OP}\right|\left|\overrightarrow{RP}\right|} = \frac{\left(\overrightarrow{ON}+\overrightarrow{NP}\right)\cdot\left(\overrightarrow{RN}+\overrightarrow{NP}\right)}{\left|\overrightarrow{OP}\right|\left|\overrightarrow{RP}\right|}$$
$$= \frac{\overrightarrow{NP}\cdot\overrightarrow{NP}+\overrightarrow{NP}\cdot\overrightarrow{RN}}{\left|\overrightarrow{OP}\right|\left|\overrightarrow{RP}\right|}$$

Note that we use $\overrightarrow{ON}\cdot\overrightarrow{RN} = \overrightarrow{ON}\cdot\overrightarrow{NP} = 0$. We can simplify the above equation and express

$$D = \frac{\overrightarrow{NP}\cdot(\overrightarrow{NP}+\overrightarrow{RN})}{\left|\overrightarrow{OP}\right|\left|\overrightarrow{RP}\right|} = \frac{\overrightarrow{NP}\cdot\overrightarrow{RP}}{\left|\overrightarrow{OP}\right|\left|\overrightarrow{RP}\right|}$$
$$= \frac{\left|\overrightarrow{NP}\right|\cos\alpha}{\left|\overrightarrow{OP}\right|} \leq \frac{\left|\overrightarrow{NP}\right|}{\left|\overrightarrow{OP}\right|}$$

where α represents the angle between $\overrightarrow{NP}$ and $\overrightarrow{RP}$ vectors. Now, $\frac{\left|\overrightarrow{NP}\right|}{\left|\overrightarrow{OP}\right|}$ is equal to the inner product between the unit-vectors along $\overrightarrow{NP}$ and $\overrightarrow{OP}$. Hence, we deduce that the modified excitation vector $[V_0]^H$ has the largest inner product; hence, the lowest angular deviation from the quiescent excitation vector $[V]^H$.

REFERENCES

[1] Mailloux, R. J., *Phased Array Antenna Handbook*, 2nd ed., Chapter 3, Artech House, 2005.

[2] Haupt, R., "Null synthesis with phase and amplitude controls at the subarray outputs," *IEEE Transactions on Antennas and Propagation*, Vol. 33, No. 5, 505–509, May 1985.

[3] Haupt, R. L., "Adaptive nulling in monopulse antennas," *IEEE Transactions on Antennas and Propagation*, Vol. 36, No. 2, 202–208, Feb. 1988.

[4] Kogan, L., "A minimum gradient algorithm for phased-array null formation," *Radio Science*, Vol. 40, No. 2, RS2S90, 2005.

[5] Sayidmarie, K. H. and J. R. Mohammed, "Performance of a wide angle and wide band nulling method for phased arrays," *Progress In Electromagnetics Research M*, Vol. 33, 239–249, 2013.

[6] Steyskal, H., R. Shore, and R. Haupt, "Methods for null control and their effects on the radiation pattern," *IEEE Transactions on Antennas and Propagation*, Vol. 34, No. 3, 404–409, Mar. 1986.

[7] Yuen, S. M., "Algorithmic, architectural, and beam pattern issues of sidelobe cancellation," *IEEE Transactions on Aerospace and Electronic Systems*, Vol. 25, No. 4, 459–472, Jul. 1989.

[8] Liu, H., A. Ghafoor, and P. H. Stockmann, "Application of Gram-Schmidt algorithm to fully adaptive arrays," *IEEE Transactions on Aerospace and Electronic Systems*, Vol. 28, No. 2, 324–334, Apr. 1992.

[9] Rice, J. R., "Experiments on Gram-Schmidt orthogonalization," *Mathematics of Computation*, Vol. 20, No. 94, 325–328, 1966.

[10] Gabriel, W., "Using spectral estimation techniques in adaptive processing antenna systems," *IEEE Transactions on Antennas and Propagation*, Vol. 34, No. 3, 291–300, Mar. 1986.

[11] Subbaram, H. and K. Abend, "Interference suppression via orthogonal projections: A performance analysis," *IEEE Transactions on Antennas and Propagation*, Vol. 41, No. 9, 1187–1194, Sep. 1993.

[12] Ellingson, S. W. and G. A. Hampson, "A subspace-tracking approach to interference nulling for phased array-based radio telescopes," *IEEE Transactions on Antennas and Propagation*, Vol. 50, No. 1, 25–30, Jan. 2002.

[13] Bhattacharyya, A. K., *Phased Array Antennas: Floquet Analysis, Synthesis, BFNs and Active Array Systems*, John Wiley & Sons, 2006.

[14] Bucci, O. M., G. Franceschetti, G. Mazzarella, and G. Panariello, "A general projection approach to array synthesis," in *Digest on Antennas and Propagation Society International Symposium*, 146–149, San Jose, CA, USA, 1989.

[15] Vescovo, R., "Power pattern synthesis for antenna arrays with null constraints in the near-field region," *Microwave and Optical Technology Letters*, Vol. 44, No. 6, 542–545, Mar. 2005.

[16] Vescovo, R., "Consistency of constraints on nulls and on dynamic range ratio in pattern synthesis for antenna arrays," *IEEE Transactions on Antennas and Propagation*, Vol. 55, No. 10, 2662–2670, Oct. 2007.

[17] Sattari, P. and N. Hejazi, "Array pattern null steering using genetic algorithm by element position perturbations," in *2008 Canadian Conference on Electrical and Computer Engineering*, 000 423–000 428, Niagara Falls, ON, Canada, May 2008.

[18] Panigrahi, S., H.-T. Chou, and C.-Y. Chang, "Radiation pattern nulling in phased array antennas using superior discrete fourier transform and Dolph-Tschebyscheff based synthesis techniques," *Radio Science*, Vol. 57, No. 4, 1–14, Apr. 2022.

[19] Gupta, A., M. Kumari, M. Sharma, M. H. Alsharif, P. Uthansakul, M. Uthansakul, and S. Bansal, "8-port MIMO antenna at 27 GHz for n261 band and exploring for body centric communication," *PLoS ONE*, Vol. 19, No. 6, e0305524, 2024.

[20] Chaparala, R., S. Imamvali, S. Tupakula, K. Prakash, S. Bansal, M. M. Ismail, and A. J. A. Al-Gburi, "Spoof surface plasmon polaritons-based feeder for a dielectric rod antenna at microwave frequencies," *Progress In Electromagnetics Research M*, Vol. 129, 23–32, 2024.

[21] Strang, G., *Linear Algebra and Its Applications*, Academic Press, New York, 2000.